Forward Modeling of Applied Geophysics Methods Using Comsol and Comparison with Analytical and Laboratory Analog Models

S.L. Butler[a,*], G. Sinha[a]

[a]*Department of Geological Sciences, University of Saskatchewan, 114 Science Place, Saskatoon, SK, S7N 5E2, Canada*

Abstract

Forward modeling is useful in geophysics both as a tool to interpret data in a research setting and as a tool to develop physical understanding in an educational setting. Gravity, magnetics, resistivity and induced polarization are methods used in applied geophysics to probe Earth's subsurface. In this contribution, we present forward models of these geophysical techniques using the finite-element modeling package, Comsol. This package allows for relatively easy implementation of these models and, as part of the AC/DC module, allows for exterior boundaries to be placed at infinity: a boundary condition that is frequently encountered in geophysics. We compare the output of the finite-element calculations with analytical solutions and, for the resistivity method, with laboratory scale analog experiments and demonstrate that these are in excellent agreement.

Keywords: gravity magnetics resistivity finite element

1. Introduction

The gravity, magnetic, resistivity and induced polarization (IP) techniques are geophysical methods used to infer the structure and composition of Earth's subsurface from surface or airborne measurements (*Telford et al*, 1990). Forward modeling of these techniques is useful, both because model

*Corresponding author. Fax:+1-306-966-8593

Email addresses: sam.butler@usask.ca (S.L. Butler), gunjan.sinha@usask.ca (G. Sinha)

parameters can be varied in order to fit observations as part of an inversion routine, and because physical intuition can be developed when model parameters are varied by students. Most forward potential fields models are based on integral equations where relatively simple formulas can be used when the anomalous density and magnetization distributions are represented in terms of polygons. The formulas were derived for 2D gravity and magnetics by *Talwani et al.* (1959) and *Talwani and Heirtzler* (1964) and for arbitrarily shaped 3D objects by *Talwani and Ewing* (1960) and *Talwani* (1965). 2.5 D models, where the anomalous density or magnetization is of finite length along strike, are popular and the 'end' correction formulas for these were derived by *Shuey and Pasquale* (1973) and *Rasmussen and Pedersen* (1979). The popular commercial software package GMsys (GMsys User's Guide, 2004) is based on these integral formulas. In this paper, the forward gravity and magnetics problems will be addressed by solving Poisson's equations with the appropriate boundary conditions. The numerical solution of Poisson's equation to determine the gravitational acceleration from a density distribution was used previously by *Zhang et al.* (2004) and *Farquharson and Mosher* (2009) and a finite volume discretization of the appropriate form of Maxwell's equations was used by *Lelièver and Oldenburg* (2006) to solve for the anomalous magnetic field due to a given magnetic susceptibility distribution. An advantage of the solution of Poisson's equation is that the potential is computed everywhere and does not need to be computed again if a new point of investigation is selected.

Resistivity modeling consists of solving Laplace's equation with source terms representing the current electrodes and appropriate boundary conditions. Published models of the resistivity method include models that are discretized based on finite difference (e.g., *Dey and Morrison*, 1979; *Zhoa*, 1996), finite element (e.g., *Coggon*, 1971; *Pridmore et al.*, 1980; *Rücker et al.*, 2006; *Ren and Tang*, 2010) finite volume (e.g., *Pidlisecky and Knight*, 2008) and integral equation based models (e.g., *Ma*, 2002).

Comsol Multiphysics (*Comsol Multiphysics Users' Guide*, 2009) is a general finite element modeling environment. While previous forward modeling efforts used specialized software for each geophysical method, in this paper, we demonstrate that a single flexible modeling tool can be used for all of the methods. Comsol allows users to develop complex numerical models with different geometries and multiple governing equations quickly using a GUI. As will be shown in the subsequent sections, models of the above mentioned geophysical techniques can be quickly implemented in Comsol and, because

of Comsol's multiphysics capability, many different techniques can be modeled simultaneously for the same anomaly geometry. The AC/DC module of Comsol contains the capability to model boundaries at infinite separation from the model domain which is the most common boundary condition encountered in geophysical problems. We will demonstrate the effectiveness of these infinite boundaries by comparing Comsol's solutions with analytical solutions.

Cardiff and Kitanidis (2008) recently showed how Comsol can be used to calculate adjoint state-based sensitivities for inverse modeling in hydrogeology while *Kalavagunta and Weller* (2005) used Comsol to calculate geometrical factors for laboratory scale resistivity experiments. Other cases where researchers have used Comsol to model electrical geophysical phenomena include *Park et al.* (2010) who modeled controlled source electromagnetics (CSEM), *Volkmann et al.* (2008) who developed a microscopic model of the frequency-domain induced polarization effect, *Stoll* (2005) who modeled the bore-hole resistivity method and *Braun et al.* (2005) who modeled the propagation of electromagnetic waves in a conducting medium with application to magnetic resonance sounding.

In what follows, we will first present the theory, implementation and results for a gravity model in Comsol and compare its results with an analytical solution. Subsequently, we will present similar sections for magnetics, resistivity and induced polarization. Following this, we will present a section analyzing the accuracy of the gravity and resistivity calculations as a function of various model parameters.

2. Methods, Theory and Results

In all of the models presented here, tetrahedral elements were used and potentials were represented using quadratic Lagrange basis functions except for two simulations listed in section 3. All of the calculations were carried out on a desktop PC using a single 2.87 GHz Intel Xeon processor. Comsol has a number of linear solvers to choose from. The method of conjugate gradients is the default solver for the electrostatics, magnetostatics and conductive media modules that were used in this study and this solver was used in all of the calculations except for the induced polarization calculations. Induced polarization calculations required the use of complex numbers which is not supported by the conjugate gradient solver in Comsol so the UMFPACK was chosen for these calculations instead. The models were initially implemented

using Comsol 3.5. Some of the models were tested and found to work similarly with some modifications in Comsol 4.2.

2.1. Gravity

Variations in subsurface density produce small variations in the vertical component of the acceleration due to gravity that can be measured at Earth's surface. Comsol does not have a built-in gravity calculation module. However, it does have an electrostatics module. Since gravity and electrostatics are both governed by Poisson's equation, a gravity model can be created from an electrostatics model by changing the value of the electrical permittivity. Poisson's equation relating the gravitational potential, U in J kg^{-1} , to the mass density distribution, ρ in kg m^{-3} , is

$$\nabla^2 U = -4\pi G\rho \tag{1}$$

where $G = 6.67 \times 10^{-11}$ J m kg^{-2} is the universal gravitational constant (e.g., *Telford et al.*, 1990). Here and throughout the rest of the paper, MKS units will be used. The Poisson equation in electrostatics relating electrical potential, V in Volts, to the charge density distribution, ρ_c in C m^{-3}, is

$$\nabla^2 V = \frac{-\rho_c}{\epsilon} \tag{2}$$

where ϵ is the electrical permittivity (e.g., *Jackson*, 1998). By setting $\epsilon = \frac{1}{4\pi G}$ and setting $\rho_c = \rho$ and $V = U$ a model for gravitational potential energy is easily produced.

In order to test the model, a cylinder with radius, a=1000 m, and density contrast with the surrounding material, $\Delta\rho = 100$ kg m^{-3}, was used. The geometry is shown in figure 1a. The cylinder lies horizontally along the y axis at mid-height and in the middle in the x direction in a cubic solution domain that is 10 km on a side. The rectangular prisms along all of the outer faces, edges and corners are 2 km thick and are used as infinite elements. The infinite elements are set to stretch the coordinates to infinity in particular directions. The corner infinite elements are stretched in all three directions while the edge infinite elements are stretched in the two directions that are normal to the edge faces while the face infinite elements are stretched only in the direction normal to the face.

The finite element mesh consisted of 153 723 tetrahedral elements. For comparison, another calculation was run in which the outer 2 km rectangular

prisms that were infinite elements in the previous calculation were simply regular parts of the computational domain. In this latter case, a constant potential, $U = 0$, was imposed as a boundary condition on all of the outer boundaries (at $x, y, z = \pm 7000$ m). Calculating the solution used 635 Mbytes of memory and required 55 s when no infinite elements were used and 84 s when infinite elements were used.

Profiles of the vertical component of gravitational acceleration, perpendicular to the long axis of the cylinder at 2 and 4 km height, above the centre of the cylinder in the y direction, are plotted in figure 1b. The dashed line is plotted from the analytical solution for the vertical component of gravity from a cylinder:

$$g_{zcyl} = \frac{2\pi G \Delta \rho a^2 z}{x^2 + z^2}. \tag{3}$$

The solid and dotted lines are plotted from numerical solutions. The solid line was calculated for a model for which the infinite elements were employed and the density anomaly extended to $y = \pm\infty$ while the dotted line did not use infinite elements so the cylinder stopped at ± 7 km. As can be seen, the numerical solution with infinite elements agrees very well with the analytical solution at both z=2 and 4 km. Evaluating g_z at different values of z mimics the effect of the cylinder being placed at different depths in the Earth or of the measurement sensor being at different altitudes. The well-known effect that gravity anomalies have reduced amplitude and become broader with distance to the source (*Telford*, 1990) can also be clearly seen. The numerical solution without infinite elements can be seen to have an amplitude that is too small, particularly for the $z = 4$ km case. The cause of the reduced amplitude is both due to the potential being forced to 0 for $x < \infty$ by the boundary condition and because the cylinder has only a finite length. A calculation with infinite elements but for which the cylindrical mass anomaly stops at $y = \pm 5$ km was also carried out (not shown) which had a similar amplitude to the case with no infinite elements which indicates that the latter effect is more significant. The larger discrepancy with height can be understood by the fact that as the observer moves farther from the anomaly, the effects of the mass that are far away laterally become increasingly important.

Although the example presented here used a simple cylindrical anomaly for the purpose of comparison with an analytical solution, arbitrarily complicated mass density distributions can be modelled. Comsol has the capability to import CAD files and in the future we intend to import digital elevation models for the purpose of computing terrain corrections.

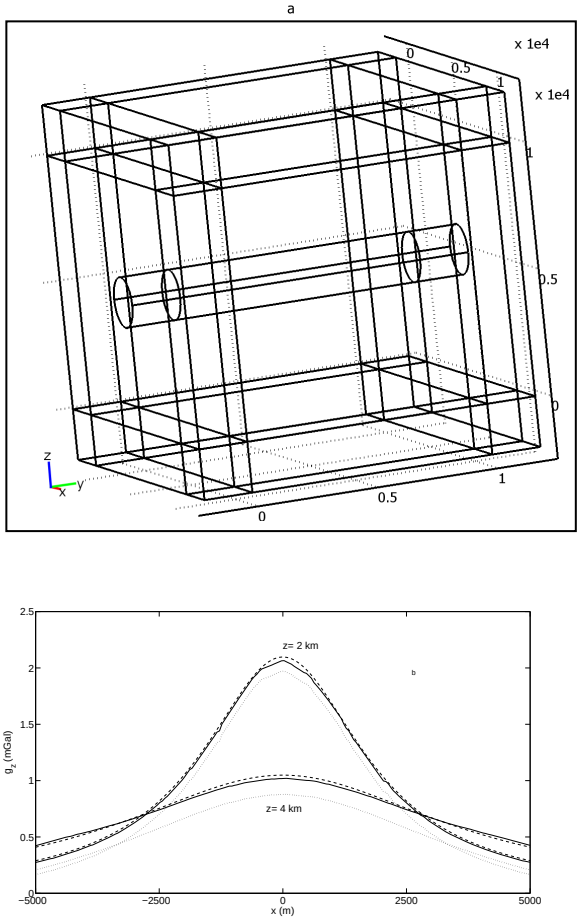

Figure 1: a) The solution geometry. Distance units are in 10^4 m. The central cylinder has anomalous density $\Delta\rho$. The outer rectangular prisms of thickness 2 km are "infinite-elements" that place the outer boundary effectively at infinity. b) Profiles of g_z at heights 2 and 4 km above the cylinder along the x axis and over the centre of the cylinder. Solid, dotted and dashed lines indicate numerical solutions with and without infinite elements and the predictions of equation 3

2.2. Magnetics

Small variations in the magnetic field measured above the Earth's surface are caused by variations in the degree of magnetization in Earth's crust. The variations in the degree of magnetization are, in turn, caused by differences in the magnetic susceptibility between different Earth materials.

In the absence of free currents and time varying magnetic and electric fields, the magnetic field $\mathbf{H}$ in A m^{-1} can be written as the gradient of a scalar potential, V_m (measured in C s^{-1}). It can be shown that for the case of materials whose magnetization is linearly related to the strength of the magnetic field, $\mathbf{M} = k\mathbf{H}$, where $\mathbf{M}$ is magnetization in A m^{-1}and k (dimensionless) is magnetic susceptibility, the magnetic scalar potential can be solved from the following equation (*Jackson*, 1999).

$$\nabla \cdot [(1 + k)\nabla V_m] = 0. \tag{4}$$

Equation 4 was solved in a cubic domain of size 40 by 40 m where $k = 0$ except in a target object where $k > 0$ using the magnetostatics capability in the AC/DC module. The normal component of the magnetic field was specified on all boundaries and was constant over the boundaries to mimic the effects of Earth's core field. The solution domain consisted of 105 335 tetrahedral finite elements. The solution required 689 Mbytes of memory and took 36 s to run. Infinite elements were not used when modeling magnetics as they were not found to work well when the solution does not go to 0 at infinity.

As a test of the model, a sphere of radius 1 m with constant magnetic susceptibility $k = 1000$ was used in the centre of the model. A sphere in a constant external field will have a constant magnetization and a sphere with constant magnetization has the same magnetic field as a magnetic dipole located at its centre. The horizontal, $H_x - H_{xext}$, and vertical, $H_z - H_{zext}$, components of the anomalous magnetic field calculated from the numerical model 2 m above the centre of the sphere are plotted along a line where $y = 0$ in figure 2 (solid lines) which are compared with the analytical expressions for a magnetic dipole from equations 5. H_{xext} and H_{zext} represent the x and z components of the externally imposed magnetic field. The analytical expression for the horizontal and vertical components of a dipole field are given by (e.g., *Telford et al.*, 1990)

$$H_x = \frac{m}{4\pi} \frac{(2x^2 - z^2)\cos I - 3xz \sin I}{(x^2 + z^2)^{5/2}}$$

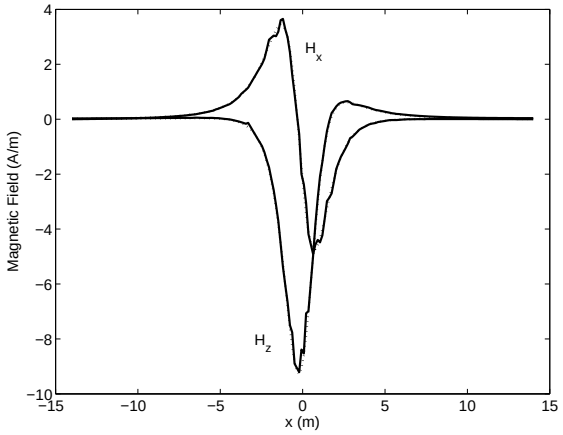

Figure 2: Profiles of anomalous H_x and H_z calculated from the numerical model (solid line) and from equations 5 (dotted line) along a line where $z = 2$ m and $y = 0$.

$$H_z = -\frac{m}{4\pi}\frac{(2z^2 - x^2)\sin I - 3xz\cos I}{(x^2 + z^2)^{5/2}} \tag{5}$$

where $m = k_{eff}|\mathbf{B_{ext}}|V/\mu_0$ is the dipole moment and the effective permeability for an object with demagnetization is given by $k_{eff} = k/(1 + kN_{geom})$ where the demagnetization factor, $N_{geom} = 1/3$, for a sphere. In the above expression, I is the magnetic inclination which was set equal to 63.4^o (corresponding to 45^o magnetic latitude) and $|\mathbf{B_{ext}}|$ is the magnitude of the external magnetic B field which was set to 50 μT. As can be seen, except for some small amplitude numerical noise, the numerical solution is in perfect agreement with the analytical expression. Because $k >> 1$ in this calculation, $k_{eff} \approx N_{geom}^{-1}$ and the amplitude of the anomalous field is significantly less than it would have been if the effects of demagnetization were not present.

A further comparison was made with the results of *Lelièvre and Oldenburg* (2006) where a prolate ellipsoidal object of semimajor axis 9 m and semiminor axes of 3 m of anomalous susceptibility was placed in the middle of the solution domain and oriented with its long axis horizontal. An external field of magnitude 50 μT and inclination $I = 58.3^o$ was applied with its horizontal component parallel to the long axis of the ellipsoid. For this simulation, the solution domain was increased in size to a cube with 80 m side lengths because of the large size of the magnetized object. Profiles of total field anomaly (the

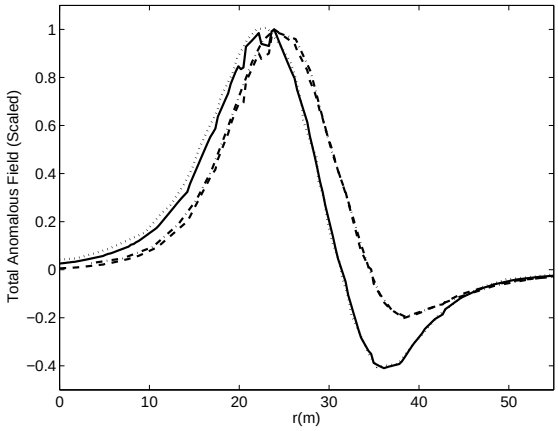

Figure 3: Profiles of the total field anomaly over a prolate ellipsoidal object of anomalous magnetic susceptibility. Dash-dot and dashed lines are from calculations with $k = 10^{-3}$ from *Lelièvre and Oldenburg* (2006) and from this study, respectively, while dotted and solid lines are from calculations with $k = 10$ from *Lelièvre and Oldenburg* (2006) and from this study.

magnitude of the total magnetic field minus the magnitude of the background field) are plotted at a height 8 m above the object and parallel to its long axis in figure 3. The total field anomaly is typically what is measured in exploration geophysics surveys. The dashed and solid lines are total field anomalies calculated from the present model with $k = 10^{-3}$ and $k = 10$ while the dash-dotted and dotted lines are the results of *Lelièvre and Oldenburg* (2006) with the same magnetic susceptibilities. As can be seen, the current model agrees very well with the results of *Lelièvre and Oldenburg* (2006). The curves have been normalized so that their maximum amplitudes are 1. *Lelièvre and Oldenburg* (2006) reported the ratio of the maximum amplitude of the curve calculated with $k = 10$ to that with $k = 10^{-3}$ to be 2225 which is identical to what we calculated. The fact that the maximum amplitude does not scale linearly with the magnetic susceptibility arises due to the effects of demagnetization. *Lelièvre and Oldenburg* (2006) also reported that for the $k = 10$ case, the magnetization had an inclination angle of 31.7^o degrees while we calculated 31.5^o.

The effects of demagnetization were further investigated using a 1 m by 1 m by 15 m rectangular prism of anomalous magnetic susceptibility. The geometry can be seen as the black lines in figures 4a and b. The rod was cen-

tered in the solution domain with its long axis parallel to the x axis. The external magnetic **B** field was specified with $[x, y, z]$ components $[22.4, 0, -44.7]$ μT to mimic Earth's magnetic field at latitude 63.4^o in the northern hemisphere. In figure 4a we show the results of a calculation with magnetic susceptibility $k = 1$, a value similar to an object with a high magnetite concentration. The red lines are magnetic field lines while the cones indicate the direction of magnetization and the colour contour plot shows a slice of the total field anomaly which is plotted on a surface of constant height, indicating what would be measured in the field over such an anomaly. As can be seen, for this low value of magnetic susceptibility, the bar is magnetized roughly parallel to the external field. The total field anomaly shows a high to the south and a low to the north which is typical of magnetic anomalies measured in the northern hemisphere (*Reynolds*, 1997).

Figure 4b shows the results of an identical calculation except that the magnetic susceptibility has been increased to 1000, a value appropriate for an iron bar. As can be seen, although the external magnetic field is at 45^o to the long axis of the bar, the bar is now magnetized parallel to its long axis because of the effects of demagnetization. Comparison of the total field anomalies shown in figure 4a and b also reveals that the magnetic field amplitude is not scaling linearly with the magnetic susceptibility and that the pattern of the total field anomaly is significantly different. As can be seen, the low to the north (positive x direction) is now much more prominent. Figure 3 also shows an increase in the prominence of the northern low in the model with large susceptibility.

Although not used in the example shown here, the model has the capability to include effects due to remnant magnetization and more complicated geometry. Comsol supplies an example model of magnetic prospecting where the magnetic field can be calculated on an uneven surface simulating real topography.

2.3. Resistivity

The resistivity method involves injecting electrical current into the ground between one pair of electrodes and measuring the electrical potential between another electrode pair. For a given electrode geometry, an "apparent resistivity", ρ_a in Ω m, can be determined from

$$\rho_a = k_g \frac{\Delta V}{I} \tag{6}$$

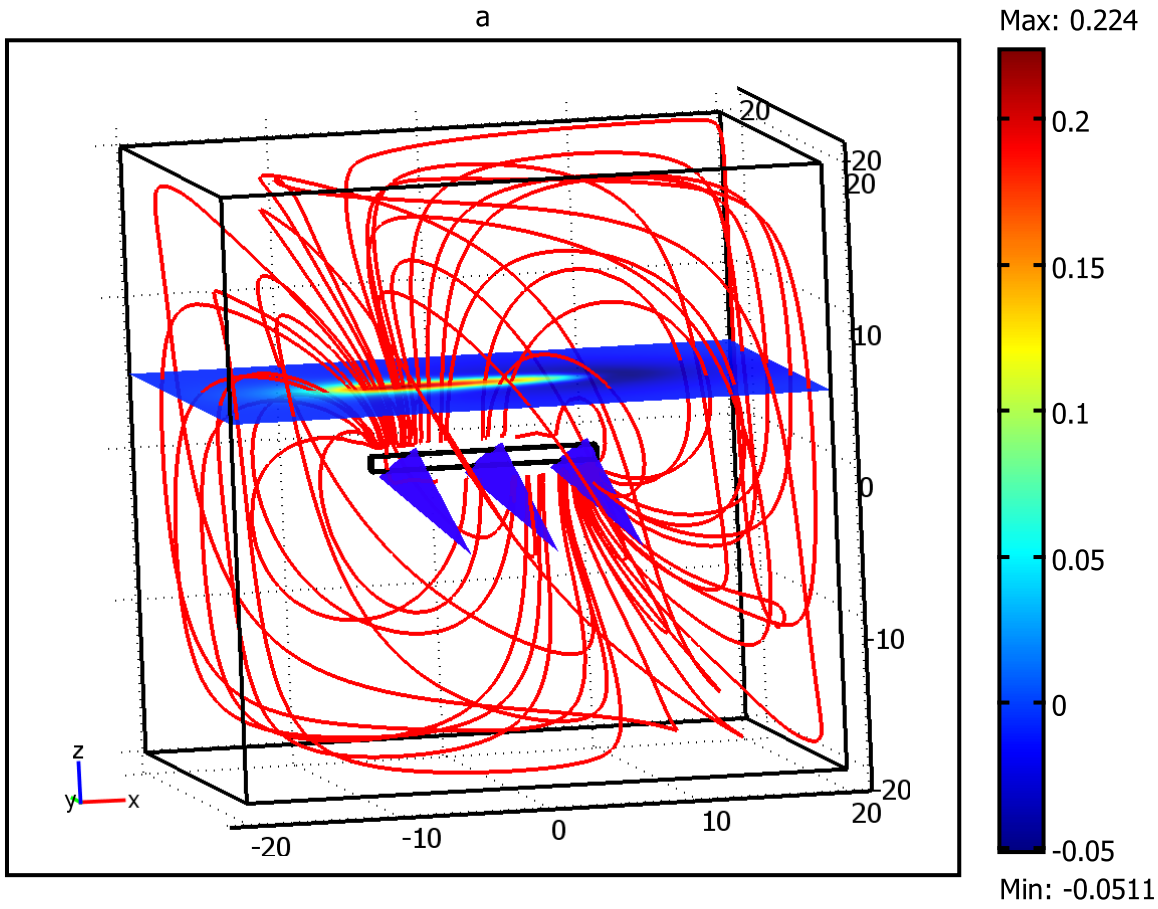
a
Max: 0.224
0.2
0.15
0.1
0.05
0
-0.05
Min: -0.0511
20
20
10
0
-10
20
-20
-10
0
10
20
z
y
x

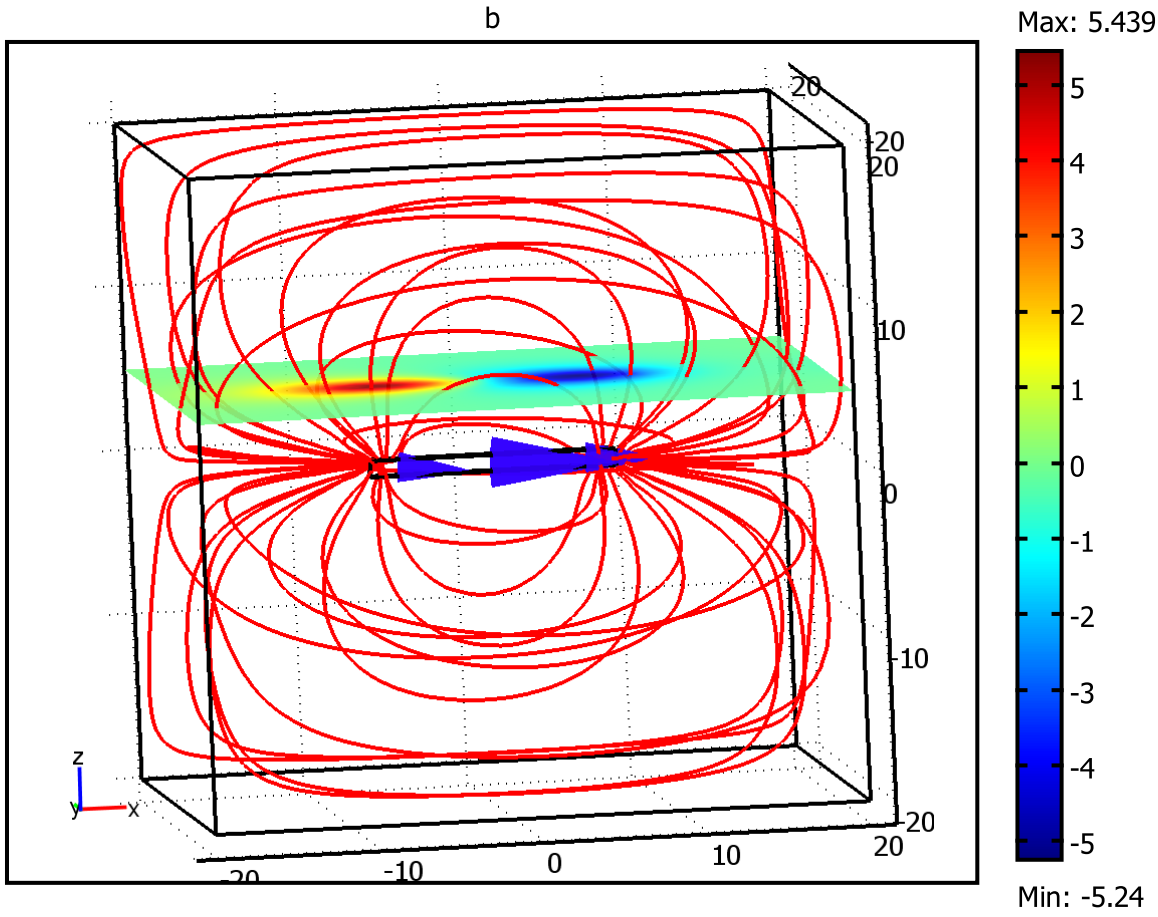

Figure 4: Red lines show magnetic field lines due to the anomalous object. Blue cones show the direction of magnetization while the colour contour plots shows the total field anomaly at a height 5 m above the anomalous rod. Units of the magnetic field are μT while distances are in m. Part a) shows the results for a calculation with $k = 1$ while in b) the results for a calculation with $k = 1000$ are shown.

where ΔV is the difference in electrical potential between the potential electrodes in Volts, I is the injected current in Amps and k_g (measured in m) is the geometrical factor of the array that depends only on the relative positions of the electrodes. The apparent resistivity is the resistivity that an infinite half space of constant resistivity would have in order to give the same measured ΔV for a given injected current. If apparent resistivity changes with a change in the lateral array position or with a change in the array spacing, there must be a lateral or vertical change in the resistivity of the ground (*Telford*, 1990).

A DC conductive media module exists in Comsol that solves

$$\nabla \cdot \sigma \nabla V = 0, \tag{7}$$

where σ is the electrical conductivity of the ground which is the reciprocal of the resistivity. Electrical current density, $\mathbf{J}$ in A m^{-2}, is given by $\mathbf{J} = -\sigma \nabla V$. Current electrodes were modelled by specifying point current sources at the surface of the model. The rest of the top surface boundary was made electrically insulating, $\nabla V \cdot \mathbf{n} = 0$, where $\mathbf{n}$ is the normal to the surface. As a test of the method, the model results were compared with those of a laboratory scale resistivity model consisting of a 14 cm deep water tank of lateral dimensions 1 m by 40 cm. In order to model conduction in the water tank, a model domain with dimensions equal to the laboratory tank was chosen and the side walls and bottom of the domain were made electrically insulating. In the laboratory model investigation, the electrodes were thin copper wires that just penetrated the top surface of the water so that the current electrodes approximate point current sources. The electrodes were set up in the Schlumberger array geometry and the current electrode spacing was increased in steps, mimicking a "depth sounding". As the spacing between the current electrodes increases, current lines are constrained to a greater degree by the bottom and sides of the tank increasing the apparent resistivity. In the numerical model, the potential was calculated everywhere in the model domain and the potentials at the same positions as in the laboratory model were determined in post-processing. The apparent resistivity was then calculated using equation 6 once k_g was calculated for the given survey geometry. In figure 5a the magenta lines are stream lines of electrical current density showing current flowing from one current electrode to the other while the surface plot shows the electrical potential at mid-depth in the tank.

In figure 5b, a line plot of the voltage calculated along the top is shown for calculations where the current electrodes were placed at ± 0.15 m and in-

finite elements were used on the sides and bottom of the domain. At a point current source, the potential is infinite which can only be approximated in numerical methods. The dotted line indicates the potential from a solution employing 14 435 roughly equally spaced finite elements while the solid line employed 55 364 finite elements. The dashed line shows the analytical solution. It can be seen that the solution employing a larger number of elements better approximates the potential in the vicinity of the current electrode. Further simulations employing a refined grid around the current electrodes gave potentials that were indistinguishable from the analytical expression when plotted as in figure 5b. The apparent resistivity was calculated using the potential measured at some distance from the current electrodes and was not generally found to be significantly affected by the mesh resolution. In section 3 we present a further analysis of the effects of model resolution.

In figure 6 we show the apparent resistivity as a function of half of the current electrode spacing, $AB/2$, for a Schlumberger array. The apparent resistivity has been normalized by the resistivity of the water. The + symbols represent laboratory data while the open circles represent the results of the numerical simulations with insulating side and bottom boundary conditions. As can be seen, the numerical simulations are in excellent agreement with the laboratory data. The analytical expression for the apparent resistivity of an infinite half space with two vertical layers with contact at depth z where the lower layer is infinitely resistive for a Schlumberger array is

$$\rho_a = [1+\frac{AB+MN}{MN}\sum_{m=1}^{\infty}(1+(\frac{4mz}{AB-MN})^2)^{-0.5}-\frac{AB-MN}{MN}\sum_{m=1}^{\infty}(1+(\frac{4mz}{AB+MN})^2)^{-0.5}] \tag{8}$$

(*Telford et al.*, 1990). The analytical solution gives the results represented by the dashed line when the interface is at a depth of 14 cm. This situation can be modeled numerically by using infinite boundaries on the side walls but maintaining the bottom boundary as electrically insulating. The results of these numerical simulations are shown by the asterisks. As can be seen, the numerical solutions are in very good agreement with the analytical solution. Finally, apparent resistivity for an infinite half space of constant resistivity is constant, regardless of the array spacing. This situation can be modelled by including infinite elements on the bottom boundary as well. These simulation results are indicated by the black $\times$ symbols. As can be seen, the calculated apparent resistivity remains close to a constant value of 1 indicating that the infinite boundaries are providing a good approximation of

placing the outer boundaries at infinity. The greatest discrepancy between the numerical and analytical solutions occurs when the current electrodes are close to the potential electrodes so that the potential is being measured where it is changing rapidly.

In figure 7 the results of a series of simulations are presented where two blocks of resistivity 1 Ωm and 10 Ωm are used where the contact between the blocks has a normal in the x direction and so the contact face is vertical. The model domain has dimensions 1 by 0.4 by 0.14 m as before. The position of the contact was varied in order to simulate translating a Schlumberger array across a vertical geological contact. The current electrodes were placed at ±0.15m while the potential electrodes were placed at ±0.04m. Infinite elements of thickness 0.2 m were placed on the side and bottom boundaries. On the plot, when $x = -0.5$ the entire domain has a resistivity of 10 Ω m while when $x = 0$ the left side of the domain has resistivity 1 Ω m while the right side has resistivity 10 Ω m. When $x = 0.5$ the entire domain has resistivity 1 Ωm.

The results are compared with the predictions of an analytical model based on the method of images for an infinite half-space with a vertical contact between two regions with different electrical resistivities (*Telford et al.*, 1990, equation 8.48). As can be seen, the simulations reproduce the analytical solution essentially perfectly including the counter-intuitive aspect that the apparent resistivity increases as more of the array falls within the less resistive medium when the interface is between A and M and when it is between N and B. Similar calculations were undertaken without the infinite elements and the apparent resistivity calculated from the numerical model was shifted upward by roughly 60% but many of the gross features of the variation of apparent resistivity with contact position were still correct.

2.4. Frequency Domain Induced Polarization

The frequency domain induced polarization method uses the same equipment as the resistivity method only an AC current is injected into the ground at the current electrodes while the amplitude and phase of the voltage difference between the potential electrodes is measured. In ground that exhibits an induced polarization response, the voltage measured at the potential electrodes may be phase shifted relative to the input current. The in-phase and out-of-phase components of the measured voltage can be represented as the real and imaginary parts of a complex voltage. The equation governing the frequency-domain induced polarization method is then the same as for the

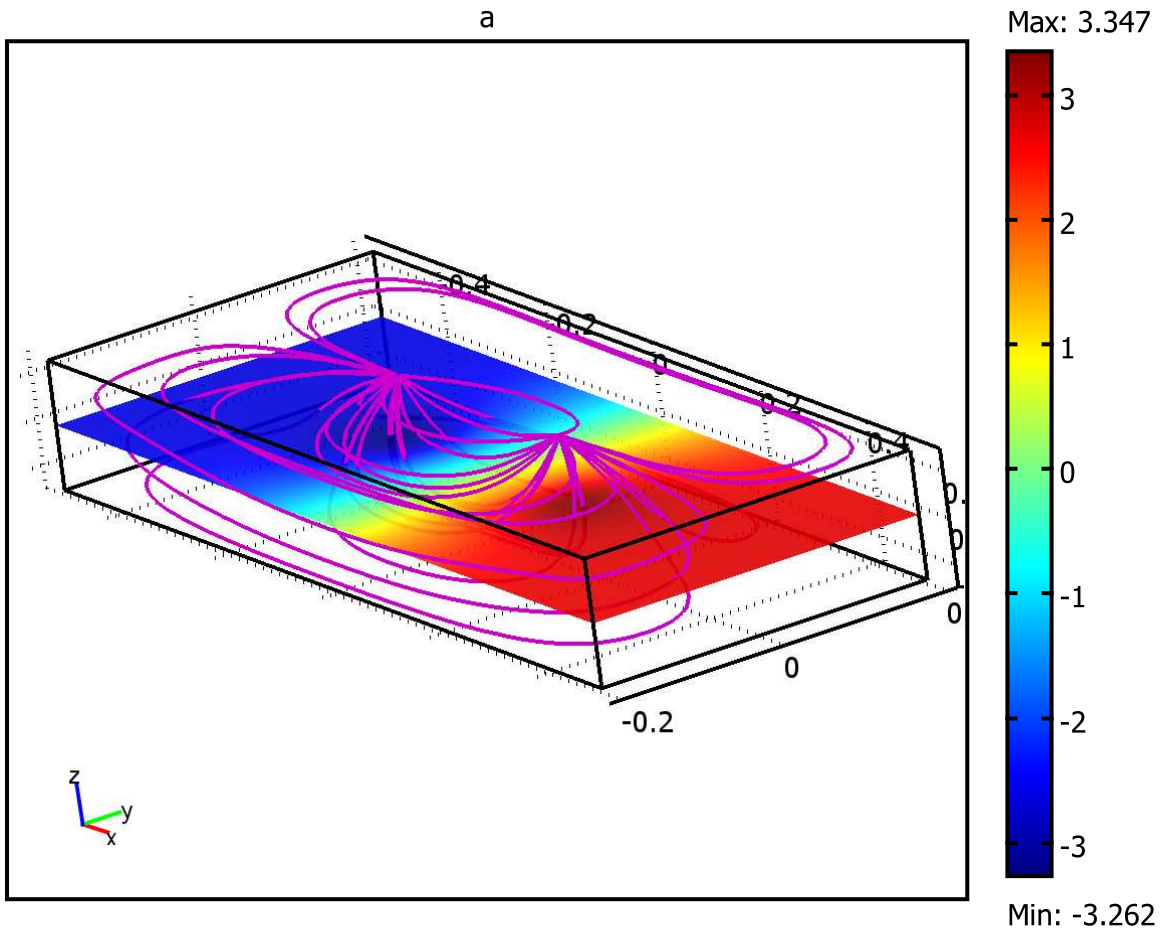
a
Max: 3.347
3
2
1
0
-1
-2
-3
Min: -3.262
-0.4
-0.2
0
0.2
0.4
-0.2
0
z
y
x

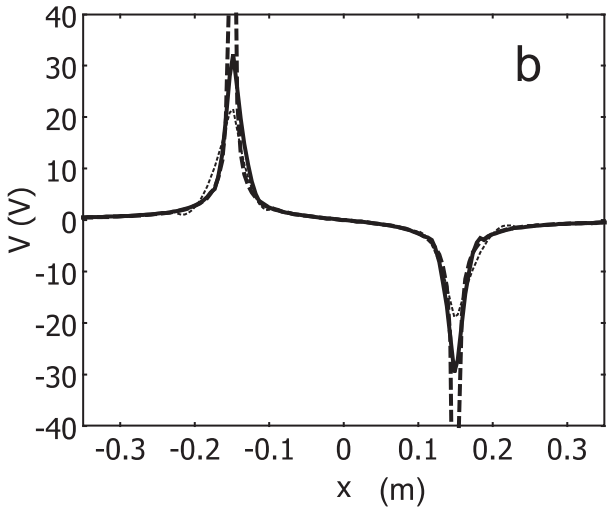

Figure 5: a) Magenta lines are streamlines of electrical current density. The surface plot shows the electrical potential at mid-depth in the domain. The current sources are placed at ± 0.15 m. Units of potential are V and dimensions are in m. b) The electrical potential along the top surface, through the current electrodes from a simulation with 14 435 finite elements (dotted line), with 55 364 finite elements (solid line) and the analytical solution (dashed line).

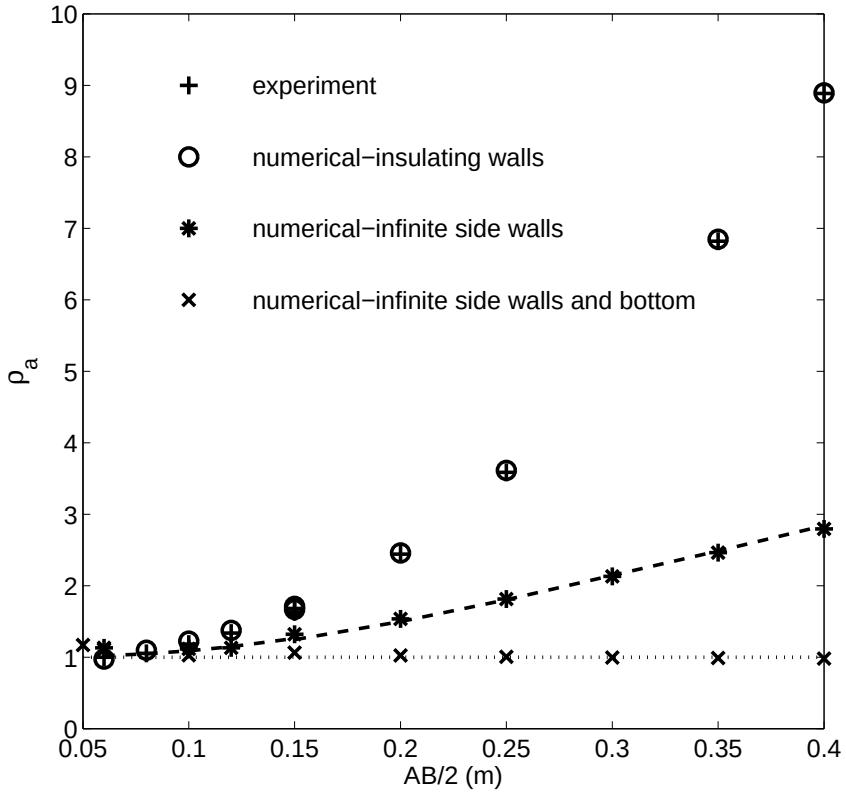

Figure 6: The normalized apparent resistivity, ρ_a, as a function of half of the current electrode spacing, $AB/2$. Open circles are numerical model results in a box with all insulating boundaries while '+' symbols are the results of laboratory experiments. The dashed line represents the analytical solution for resistivity in an infinite half space with two layers where the lower layer is infinitely resistive while the asterisks show the results of numerical solutions with infinite side walls but insulating top and bottom boundary conditions. The $\times$ symbols are from numerical simulations with infinite elements on the sides and bottom while the dotted line is a constant value of 1.

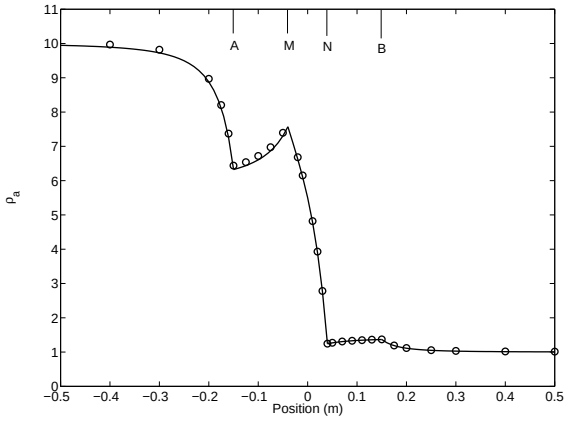

Figure 7: The apparent resistivity as a function of the position of the vertical contact between two regions with resistivities 1 and 10. The circles are the results of numerical simulations while the solid line is the analytical solution based on the method of images. The positions of the current electrodes A and B and of the potential electrodes M and N are indicated.

resistivity method (equation 7) only the electrical potential and electrical conductivity now have real and imaginary parts. The injected current is entirely real and so the phase of the voltage is measured relative to the injected current. A common model for the complex resistivity as a function of angular frequency, ω, for an Earth material that demonstrates an IP response is the Cole-Cole model:

$$\rho_a = \rho_0(1 - M(1 - \frac{1}{1 + (i\omega\tau)^c})). \tag{9}$$

The parameters ρ_0, M, c, and τ represent the DC resistivity, the "chargeability", the frequency exponent, and a time constant (*Telford et al.* 1990).

A set of simulations was undertaken with the same domain as for the resistivity simulations with a Schlumberger array with current electrodes A and B at $\pm$0.15m and potential electrodes at $\pm$0.04m. The Cole-Cole model above was input for the resistivity with parameters $M = 0.1$, $\tau = 1$s and $c = 0.25$. The real and imaginary parts of the potential difference between the two potential electrodes were calculated in post-processing and the real and imaginary parts of the apparent resisitivy were calculated using equation 6 for a number of values of the angular frequency. The magnitude of the apparent resistivity and the phase shift, ϕ, relative to the input current

were then calculated. The direct linear solver "UMFPACK" was chosen for these simulations since this solver allows for the use of complex numbers and the "allow complex output from real input" tab was selected. When using Comsol 4.2, the direct solver "MUMPS" was used. Direct solvers requires significantly more memory and solutions used 2 Gbytes to solve a mesh with 34012 tetrahedral elements and took 23.5 s. The mesh was refined in the vicinity of the current electrodes by specifying a maximum element size of 10^{-4} at these points.

In figure 8a the squares show the magnitude of the apparent resistivity as a function of frequency while the solid line shows the direct evaluation of equation 9. The numerical simulation results are shifted upward slightly compared to the direct evaluation, however, the error is significantly less than 1%. In figure 8b, the phase shift as a function of frequency is plotted and the agreement between the numerical calculation and the direct evaluation is essentially perfect. Again, more complex geometries could be investigated.

3. Accuracy Analysis and Sensitivity Study

In order to investigate the accuracy of the numerical solutions, two test cases were devised that were compared with analytical solutions. The first test case chosen was the calculation of the vertical component of gravity from an infinite horizontal cylinder as in section 2.1. The missfit was defined as

$$missfit = \frac{\int (g_z - g_{zcyl})^2 dV}{\int g_{zcyl}^2 dV}. \tag{10}$$

where the numerical integration was carried out over the volume of the domain, excluding the infinite elements and the volume of the cylinder itself. A number of simulations were undertaken with various resolution, with and without infinite elements, and with different domain sizes. The missfit for these simulations, as well as the solution time and memory usage are summarized in table 1. As can be seen, missfit decreases substantially when infinite elements are used as was also demonstrated in figure 1b while the solution time and memory usage are only weakly affected. Increasing the resolution, either by increasing the number of elements or by increasing the order of the basis functions decreases the missfit, as would be expected, but at a significant cost in solution time and memory usage. However, if the resolution used is too low, as in the simulations with only 11 312 elements

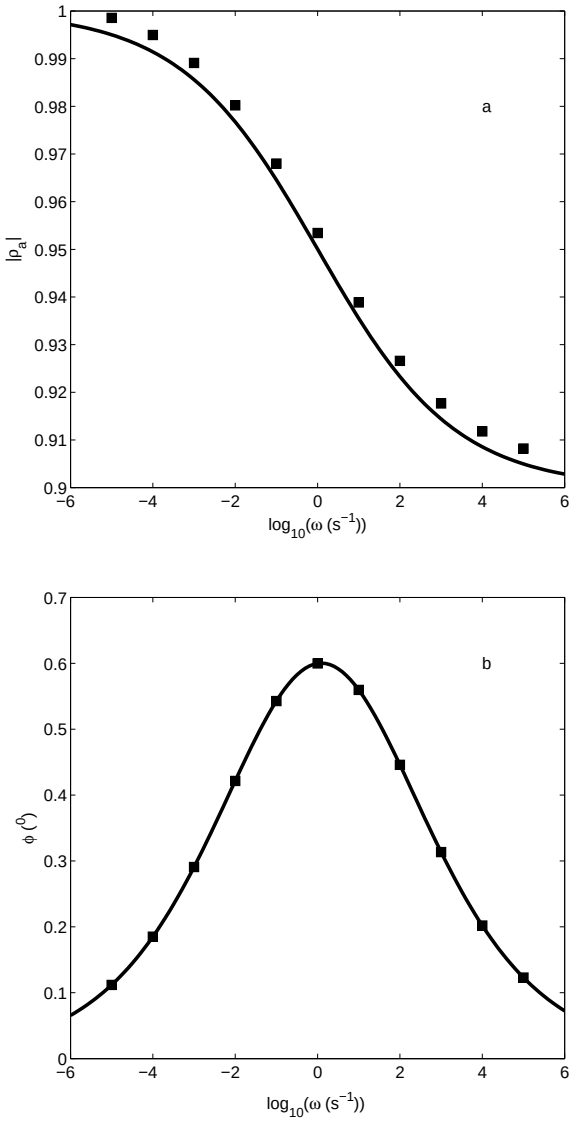

Figure 8: a) The magnitude of the apparent resistivity and b) of the phase angle of the resistivity as a function of the frequency of the current. Squares are the results of the numerical simulation while the solid lines are the direct evaluation of equation 9.

domain width (m)	# elements	element order	infinite elements	infinite element width (km)	solution time (s)	memory (Mbytes)	missfit
10000	117 372	2	yes	2000	63	540	2.2×10^{-4}
14000	117 372	2	no	-	31	540	5.0×10^{-2}
10000	421 995	2	yes	2000	457	1095	6.5×10^{-5}
10000	11 312	2	yes	2000	3.1	330	6.1×10^{-2}
10000	45 890	2	yes	2000	16.7	400	2.8×10^{-3}
10000	21 533	2	yes	2000	7.7	372	7.4×10^{-3}
10000	117 373	1	yes	2000	3.1	350	1.8×10^{-2}
10000	117 373	3	yes	2000	1190	1452	1.35×10^{-4}
20000	147 941	2	yes	4000	89	530	2.1×10^{-4}
28000	147 941	2	no	-	46	590	3.7×10^{-2}
24000	129 918	2	no	-	37.6	460	7.2×10^{-2}
20000	129 918	2	yes	2000	79	533	9.4×10^{-3}
20000	471 547	2	yes	2000	542	1041	4.0×10^{-4}
20000	479 830	2	yes	4000	536	1069	1.0×10^{-4}
10000	126 576	2	yes	4000	70	451	9.6×10^{-5}
10000	431 306	2	yes	4000	506	1069	2.8×10^{-5}
10000	420 261	2	yes	1000	407	1069	5.6×10^{-4}
10000	104 138	2	yes	1000	61	580	9.7×10^{-3}

Table 1: Summary of calculations for the gravity due to an infinite cylinder.

and the one with linear basis functions, the missfit increases significantly. When infinite elements are used, the effect of increasing the solution domain is fairly modest, indicating that the infinite elements are working well. However, changing the size of the infinite elements affects the accuracy of the solution significantly and it can be seen that the accuracy decreases significantly when the thicknesses of the infinite elements are less than 20% of the domain dimension.

The second test case involved comparing the electrical potential calculated in a resistivity calculation with constant resistivity and infinite elements placed on the sides and bottom with the analytical expression for an infinite half-space of constant resistivity, ρ, and two current sources of strength, I

and $-I$ at points (x_1, y_1, z_1) and (x_2, y_2, z_2):

$$V = \frac{I\rho}{2\pi}\left[\frac{1}{((x-x_1)^2+(y-y_1)^2+(z-z_1)^2)^{0.5}} - \frac{1}{((x-x_2)^2+(y-y_2)^2+(z-z_2)^2)^{0.5}}\right]. \tag{11}$$

The missfit in this case was defined in a manner similar to equation 10 only the analytical solution above was used and compared with the potential calculated from the numerical model. The main purpose of this second set of calculations was to investigate the effects of refining the mesh in the vicinity of the current electrodes and the results are given in table 2. The first three simulations listed were carried out to look at the effect of increasing the resolution in a uniform mesh. As can be seen, increasing resolution again increases the solution accuracy only marginally while significantly increasing the solution time and memory usage. The mesh spacing in the vicinity of a point can be varied in Comsol by specifying the maximum element size at the point. This value is given in the table under "point refinement". As can be seen, increasing the resolution near the current electrodes dramatically increases the accuracy of the solution without significantly increasing the solution time and memory usage. The last two simulations were carried out to investigate the effects of the width of the infinite elements and again, the accuracy of the solution was seen to increase significantly when the infinite elements were made larger.

4. Discussion and Conclusions

The models presented in the previous sections all took only a very short time to implement using Comsol's GUI, unlike previous models of applied geophysical techniques which require extensive time writing and testing code. This makes this modelling approach particularly useful in a classroom setting as students can develop models from the equations from start to finish. The modeling approach is also very flexible and regions with different material properties and different boundary conditions (such as the insulating walls of the resistivity tank) can be easily implemented and changed. The multiphysics capability of Comsol also allows various techniques for the same anomalous material to be modeled simultaneously and even allows for interactions between the physical phenomena although interactions are unlikely for the physical systems modeled here.

The capability to put boundaries at infinity using infinite elements is extremely useful when modeling applied geophysics techniques.

# elements	point refinent	infinite element width (m)	solution time (s)	memory (Mbytes)	missfit
20 762	no	0.4	17.5	250	1.0×10^{-2}
81 520	no	0.4	97	390	8.5×10^{-3}
431 706	no	0.4	1092	1230	3.5×10^{-3}
23 292	10^{-2}	0.4	22	262	1.4×10^{-3}
28 320	10^{-3}	0.4	20.4	373	1.55×10^{-4}
34 025	10^{-4}	0.4	24.6	347	4×10^{-5}
16 655	10^{-4}	0.4	6.3	280	1.02×10^{-4}
12 052	10^{-4}	0.4	4	270	1.57×10^{-4}
98 580	10^{-4}	0.4	106	483	2.3×10^{-5}
455 656	10^{-4}	0.4	989	1328	1.1×10^{-5}
28 903	10^{-4}	0.3	17.2	322	6.7×10^{-5}
27 318	10^{-4}	0.2	16.4	338	1.4×10^{-4}

Table 2: Summary of calculations for the potential in a resistivity calculation in an infinite half-space with two current sources.

In the future, we intend to compare measured magnetic and resistivity anomalies over objects of known geometry in the field with anomalies calculated using the models described above. We also intend to produce models of induction-based electromagnetic techniques using the AC/DC module of Comsol.

5. Acknowledgements

We would like to acknowldege Jim Merriam for his contribution to the resistivity experiments. We would also like to acknowledge reviewers Colin Farquharson and Michael Cardiff for their helpful comments that greatly improved this manuscript.

6. References

1. Braun M., Rommel I., U. Yaramanci, Modelling of magnetic resonance sounding using finite elements (FEMLAB) for 2D resistivity extension, *Proceedings of the COMSOL Multiphysics User's Conference 2005 Frankfurt.*

2. Cardiff M. and Kitanidis P.K., Efficient solution of nonlinear, underdetermined inverse problems with a generalized PDE model, *Computers and Geosciences.*, *34*, 1480-1491, 2008.
3. COMSOL Multiphysics Users Guide, Version 3.5a, COMSOL AB, Stockholm, Sweden, 2009.
4. Coggon, J. H., Electromagnetic and electric modeling by the finite element method, *Geophysics*, 36, 132155, 1971.
5. Dey A. and H.F. Morrison, Resistivity modelling for arbitrarily shaped two-dimensional structures, *Geophysical Prospecting*, 27, 106136, 1979.
6. Farquharson, C.G, Mosher, C.R.W., 2009. Three-dimensional modelling of gravity data using finite differences, *J. of Applied Geophysics*, 68, 417-422.
7. GMsys, Gravity/Magnetic Modeling Software User's Guide, Version 4.9, Northwest Geophysical Associates, Corvallis Oregon, 2004.
8. Jackson, J.D., *Classical Electrodynamics*, Wiley, New York, 1998.
9. Kalavagunta, A. and R.A. Weller, Accurate Geometry Factor Estimation for the Four Point Probe Method using COMSOL Multiphysics, *Proceedings of the Comsol Users Conference, Boston 2005.*
10. Lelièvre, P.G., Oldenburg, D.W., Magnetic forward modelling and inversion for high susceptibility, *Geophysical Journal International*, 166, 76-90, 2006.
11. Ma, Q.Z., The boundary element method for 3-D dc resistivity modeling in layered earth, *Geophysics* [0016-8033], 67, 610 -617, 2002.
12. Park J.,T. I. Bjrnar1, and B. A. Farrelly, Absorbing boundary domain for CSEM 3D modelling, *Excerpt from the Proceedings of the COMSOL Conference 2010 Paris.*
13. Pidlisecky A., and R. Knight, FW2 5D: A MATLAB 2.5-D electrical resistivity modeling code, *Computers and Geosciences*, 34, 1645-1654, 2008.
14. Pridmore, D. F.,G.W. Hohmann, S.H.Ward, and W. R. Sill, An investigation of finite-element modeling for electrical and electromagnetical data in 3D, *Geophysics*, 46, 10091033, 1980.
15. Rasmussen, R., and Pedersen, L.B., End corrections in potential field modeling, *Geophysical Prospecting*, 27, 749-760, 1979.
16. Ren, Z.Y., and Tang J.T., 3D direct current resistivity modeling with unstructured mesh by adaptive finite-element method, *Geophysics*, 75, H7-H17, 2010.

17. Reynolds, J.M., *An Introduction to Applied and Environmental Geophysics*, Wiley, New York, 1997.
18. Rücker, C., Günther, T., Spitzer, K., Three-dimensional modelling and inversion of dc resistivity data incorporating topography I. Modelling, *Geophysical Journal International*, 166, 495-505, 2006.
19. Shuey, R.T., and Pasquale, A.S., End corrections in magnetic profile interpretation, *Geophysics*, 38, 507-512.
20. Stoll J.B., FE-Modelling of Electrical Borehole Tool Responses, *Proceedings of the COMSOL Multiphysics User's Conference 2005 Frankfurt.*
21. Talwani, M., J. L. Worzel, and M. Landisman, Rapid gravity computations for two-dimensional bodies with application to the Mendocino submarine fracture zone, *Journal of Geophyical Research*, 64, 4959, 1959.
22. Talwani, M. and M. Ewing, Rapid computation of gravitational attraction of three-dimensional bodies of arbitrary shape, *Geophysics*, 25, 203225, 1960.
23. Talwani, M. and J. R. Heirtzler, Computation of magnetic anomalies caused by two-dimensional structures of arbitrary shape,*Computers in the Mineral Industries*, George A. Parks (ed.), School of Earth Sciences, Stanford University (Publc.), 464480, 1964.
24. Talwani, M., Computation with the help of a digital computer of magnetic anomalies caused by bodies of arbitrary shape, *Geophysics*, 30(5), 797817, 1965.
25. Telford, W.M., L.P. Geldart and R.E. Sheriff, *Applied Geophysics 2nd Ed.*, Cambridge U. Press, Cambridge, 1990.
26. Volkmann, J., Mohnke, O., N. Klitzsh and R. Blaschek, Microscale Modelling of the Frequency Dependent Resistivity of Porous Media, *Proceedings of the COMSOL Conference 2008 Hanover*
27. Zhang, J., Wang, C.-Y., Shi, Y., Cai, Y., Chi, W.-C., Dreger, D., Cheng, W.-B., Yuan, Y.-H., Three-dimensional crustal structure in central Taiwan from gravity inversion with a parallel genetic algorithm. *Geophysics* 69, 917-924, 2004.
28. Zhao S.K., Yedlin M.J., Some refinements on the finite-difference method for 3-D dc resistivity modeling, *Geophysics*, 61, 1301-1307, 1996.